Automatic characterization and segmentation of human skin using three-dimensional optical coherence tomography

Yasuaki Hori, Yoshiaki Yasuno

Computational Optics Group, Institute of Applied Physics, University of Tsukuba, Tennodai 1-1-1, Ibaraki, Tsukuba, 305-8573, Japan

yasuno@optlab2.bk.tsukuba.ac.jp

http://optics.bk.tsukuba.ac.jp/COG/

Shingo Sakai, Masayuki Matsumoto, Tomoko Sugawara

Kanebo Cosmetics Inc., 5-3-28 Kotobuki-Cho, Odawara, Kanagawa, Japan

Violeta Dimitrova Madjarova, Masahiro Yamanari, Shuichi Makita

Computational Optics Group, Institute of Applied Physics, University of Tsukuba, Tennodai 1-1-1, Ibaraki, Tsukuba, 305-8573, Japan

Takeshi Yasui, Tsutomu Araki

Department of Mechanical Science and Bioengineering, Graduate School of Engineering Science, Osaka University, Toyonaka, Osaka, 560-8531, Japan

Masahide Itoh, and Toyohiko Yatagai

Institute of Applied Physics, University of Tsukuba, Tennodai 1-1-1, Ibaraki, Tsukuba, 305-8573, Japan

Abstract: A set of fully automated algorithms that is specialized for analyzing a three-dimensional optical coherence tomography (OCT) volume of human skin is reported. The algorithm set first determines the skin surface of the OCT volume, and a depth-oriented algorithm provides the mean epidermal thickness, distribution map of the epidermis, and a segmented volume of the epidermis. Subsequently, an en face shadowgram is produced by an algorithm to visualize the infundibula in the skin with high contrast. The population and occupation ratio of the infundibula are provided by a histogram-based thresholding algorithm and a distance mapping algorithm. En face OCT slices at constant depths from the sample surface are extracted, and the histogram-based thresholding algorithm is again applied to these slices, yielding a three-dimensional segmented volume of the infundibula. The dermal attenuation coefficient is also calculated from the OCT volume in order to evaluate the skin texture. The algorithm set examines swept-source OCT volumes of the skins of several volunteers, and the results show the high stability, portability and reproducibility of the algorithm.

OCIS codes: (170.4500) Optical coherence tomography; (170.1870) Dermatology; (170.3880) Medical and biological imaging; (100.6950) Tomographic image processing; (110.4500) Optical coherence tomography

#10151 - $15.00 USD Received 3 January 2006; revised 20 February 2006; accepted 27 February 2006

References and links

1. D. Huang and E. A. Swanson and C. P. Lin, J. S. Schuman, W. G. Stinson and W. Chang and M. R. Hee, T. Flotte and K. Gregory and C. A. Puliafito and J. G. Fujimoto, "Optical coherence tomography," Science **254,** 1178–1181 (1991).
2. J. Welzel, "Optical coherence tomography in dermatology: a review," Skin. Res. Technol. **7,** 1–9 (2001).
3. J.M. Schmitt, M.J. Yadlowsky and R.F. Bonner., "Subsurface imaging of living skin with optical coherence microscopy," Darmatology **191,** 93–98 (1995).
4. J. Welzel, E. Lankenau, R. Birngruber and R. Engelhardt, "Optical coherence tomography of the human skin," J. Am. Acad. Dermatol. **37,** 958–963 (1997).
5. N.D. Gladkova, G.A. Petrova, N.K. Nikulin, S.G. Radenska-Lopovok, L.B. Snopova, Y.P. Chumakov, V.A. Nasonova, V.M. Gelikonov, G.V. Gelikonov, R.V. Kuranov, A.M. Sergee and F.I. Feldchtein, "In vivo optical coherence tomography imaging of human skin: norm and pathology," Skin. Res. Technol. **6,** 6–16 (2000).
6. A. Paginoni, A. Knuette, P. Welker, M. Rist, T. Stoudemaye, L. Kolbe, I. Sadiq and A.M. Kligman, "Optical coherence tomography in dermatology," Skin. Res. Technol. **5,** 83–87 (1999).
7. M.C. Pierce, J. Strasswimmer, B.H. Park, B. Cense, and J.F. de Boer, "Advances in optical coherence tomography imaging for dermatology," J. Invest. Dermatol. **123,** 458–463 (2004).
8. J.F. de Boer, T.E. Milner, M.J.C. van Gemert and J.S. Nelson, "Two-dimensional birefringence imaging in biological tissue by polarization-sensitive optical coherence tomography," Opt. Lett. **22,** 934–936 (1997).
9. J.F. de Boer, S.M. Srinivas, A. Malekafzali, Z. Chen and J. Nelson, "Imaging thermally damaged tissue by Polarization Sensitive Optical Coherence Tomography," Opt. Express **3,** 212–218 (1998), http://www.opticsexpress.org/abstract.cfm?URI=OPEX-3-6-212.
10. B.H. Park, C. Saxer, S.M. Srinivas, J.S. Nelson and J.F. de Boer, "In vivo burn depth determination by high-speed fiber-based polarization sensitive optical coherence tomography," J. Biomed. Opt. **6,** 474–479 (2001).
11. Z. Chen, T.E. Milner, S.Srinivas, X. Wang and A. Malekafzali, M.J.C. van Gemert, and J.S. Nelson, "Noninvasive imagingof in vivo blood flow velocity usingoptical Doppler tomography," Opt. Lett. **22,** 1119–1121 (1997).
12. Y. Zhao, Z. Chen, C. Saxer, S. Xiang, J.F. de Boer and J. S. Nelson, "Phase-resolved optical coherence tomography and optical Doppler tomography for imaging blood f low in human skin with fast scanning speed and high velocity sensitivity," Opt. Lett. **25,** 114–116 (2000).
13. Y. Zhao, Z. Chen, C. Saxer, Q. Shen, S. Xiang, J.F. de Boer and J.S. Nelson, "Doppler standard deviation imaging for clinical monitoring of in vivo human skin blood flow," Opt. Lett. **25,** 1358–1360 (2000).
14. S. Inomata, Y. Matsunaga, S. Amano, K. Takada, K. Kobayashi, M. Tsunenaga, T. Nishiyama, Y. Kohno, and M. Fukuda, "Possible involvement of gelatinases in basement membrane damage and wrinkle formation in chronically ultraviolet B-exposed hairless mouse," J. Invest. Dermatol. **120,** 128–134 (2003).
15. Y. Nishimori, C. Edwards, A. Pearse, K. Matsumoto, M. Kawai, and R. Marks, "Degenerative alterations of dermal collagen fiber bundles in photodamaged human skin and UV-irradiated hairless mouse skin: possible effect on decreasing skin mechanical properties and appearance of wrinkles," J. Invest. Dermatol. **117,** 1458–1463 (2001).
16. M. Suehiro, S. Hirano, K. Ikenaga, N. Katoh, H. Yasuno and S. Kishimoto, "Characteristics of skin surface morphology and transepidermal water loss in clinically normal-appearing skin of patients with atopic dermatitis: a video-microscopy study," J. Dermatol. **31,** 78–85 (2004).
17. G.L. Grove, M.J. Grove, J.J. Leyden, L. Lufrano, B. Schwab, B.H. Perry and E.G. Thorne, "Skin replica analysis of photodamaged skin after therapy with tretinoin emollient cream," J. Am. Acad. Dermatol. **25,** 231–237 (1991).
18. M. Rajadhyaksha, M. Grossman, D. Esterowitz, R.H. Webb and R.R. Anderson, "In vivo confocal scanning laser microscopy of human skin: melanin provides strong contrast," J. Invest. Dermatol. **104,** 946–952 (1995).
19. M. Vogt, A. Knuttel, K. Hoffmann, P. Altmeyer and H. Ermert, "Comparison of high frequency ultrasound and optical coherence tomography as modalities for high resolution and non invasive skin imaging," Biomed. Tech. **48,** 116–121 (2003).
20. A. F. Fercher and C. K. Hitzenberger and G. Kamp and S. Y. El-Zaiat, "Measurement of intraocular distances by backscattering spectral interferometry," Opt. Commun. **117,** 43–48 (1995).
21. Gerd Häusler and Michael Walter Lindner, " "Coherence radar" and "spectral radar" —New tools for dermatological diagnosis," J. Biomed. Opt. **3,** 21–31 (1998).
22. M. Wojtkowski, T. Bajraszewski, P. Targowski, and A. Kowalczyk, "Real-time in vivo imaging by high-speed spectral optical coherence tomography," Opt. Lett. **28,** 1745–1747 (2003), http://www.opticsinfobase.org/abstract.cfm?URI=ol-28-19-1745.
23. N. Nassif, B. Cense, B. Park, M. Pierce, S. Yun, B. Bouma, G. Tearney, T. Chen, and J. de Boer, "*In vivo* high-resolution video-rate spectral-domain optical coherence tomography of the human retina and optic nerve," Opt. Express **12,** 367–376 (2004), http://www.opticsinfobase.org/abstract.cfm?URI=oe-12-3-367.
24. Takahisa Mitsui, "Dynamic range of optical reflectometry with spectral interferometry," Jpn. J. Appl. Phys. **38,** 6133-6137 (1999).

#10151 - $15.00 USD Received 3 January 2006; revised 20 February 2006; accepted 27 February 2006

25. R. A. Leitgeb, C. K. Hitzenberger, A. F. Fercher," Performance of fourier domain vs. time domain optical coherence tomography," Opt. Express **11,** 889–894 (2003), http://www.opticsexpress.org/abstract.cfm?URI=OPEX-11-8-889.
26. Johannes F. de Boer, Barry Cense, B. Hyle Park, Mark C. Pierce, Guillermo J. Tearney and Brett E. Bouma," "Improved signal-to-noise ratio in spectral-domain compared with time-domain optical coherence tomography," Opt. Lett. **28,** 2067–2069 (2003).
27. Michael A. Choma, Marinko V. Sarunic, Changhuei Yang and Joseph A. Izatt, "Sensitivity advantage of swept source and Fourier domain optical coherence tomography," Opt. Express **11,** 2183–2189 (2003), http://www.opticsexpress.org/abstract.cfm?URI=OPEX-11-18-2183.
28. Maciej Wojtkowski, Rainer Leitgeb, Andrzej Kowalczyk, Tomasz Bajraszewski, and Adolf F. Fercher, "*In vivo* human retinal imaging by Fourier domain optical coherence tomography," J. Biomed. Opt. **7,** 457–463 (2002).
29. S. H. Yun, G. J. Tearney, B. E. Bouma, B. H. Park, and J. F. de Boer, "High-speed spectral-domain optical coherence tomography at 1.3 μm wavelength," Opt. Express **11,** 3598–3604 (2003), http://www.opticsexpress.org/abstract.cfm?URI=OPEX-11-26-3598.
30. B. H. Park, M. C. Pierce, B. Cense, S. Yun, M. Mujat, G. J. Tearney, B. E. Bouma, and J. F. de Boer, "Real-time fiber-based multi-functional spectral-domain optical coherence tomography at 1.3 μm," Opt. Express **13,** 3931–3944 (2005), http://www.opticsexpress.org/abstract.cfm?URI=OPEX-13-11-3931.
31. S. Chinn, E. Swanson, and J. Fujimoto, "Optical coherence tomography using a frequency-tunable optical source ," Opt. Lett. **22,** 340–342 (1997).
32. S. H. Yun, G. J. Tearney, J. F. de Boer, N. Iftimia, and B. E. Bouma, "High-speed optical frequency-domain imaging," Opt. Express **11,** 2953–2963 (2003), http://www.opticsexpress.org/abstract.cfm?URI=OPEX-11-22-2953.
33. Jun Zhang, Woonggyu Jung, J. Stuart Nelson and Zhongping Chen, Full range polarization-sensitive Fourier domain optical coherence tomography, Opt. Express **12,** 6033–6039 (2004), http://www.opticsexpress.org/abstract.cfm?URI=OPEX-12-24-6033.
34. Marinko V. Sarunic, Michael A. Choma, Changhuei Yang, and Joseph A. Izatt, "Instantaneous complex conjugate resolved spectral domain and swept-source OCT using 3x3 fiber couplers," Opt. Express **13,** 957–967 (2005), http://www.opticsexpress.org/abstract.cfm?URI=OPEX-13-3-957.
35. R. Huber, M. Wojtkowski, K. Taira, J. G. Fujimoto and K. Hsu, "Amplified, frequency swept lasers for frequency domain reflectometry and OCT imaging: design and scaling principles," Opt. Express **13** 3513–3528 (2005), http://www.opticsexpress.org/abstract.cfm?URI=OPEX-13-9-3513.
36. Y. Yasuno, V.D. Madjarova, S. Makita, M. Akiba, A. Morosawa, C. Chong, T. Sakai, K. Chan, M. Itoh, and T. Yatagai, "Three-dimensional and high-speed swept-source optical coherence tomography for in vivo investigation of human anterior eye segments," Opt. Express **13,** 10652–10664 (2005), http://www.opticsinfobase.org/abstract.cfm?URI=oe-13-26-10652.
37. R. Huber, M. Wojtkowski, J. Fujimoto, J. Jiang, and A. Cable, "Three-dimensional and C-mode OCT imaging with a compact, frequency swept laser source at 1300 nm," Opt. Express **13,** 10523-10538 (2005), http://www.opticsinfobase.org/abstract.cfm?URI=oe-13-26-10523.
38. S. H. Yun, C. Boudoux, G. J. Tearney and B. E. Bouma, "High-speed wavelength-swept semiconductor laser with a polygon-scanner-based wavelength filter," Opt. Lett. **28,** 1981–1983 (2003).
39. William J. Cunliffe, "Histology," in Acne, (Martin Dunitz Ltd., London, UK, 1989), pp. 93–114.
40. American National Standards institute, "American National Standard for the Safe Use of Lasers ANSI Z136.1-2000," American National Standards institute, New York (2000).
41. J. Weissman, T. Hancewicz, and P. Kaplan, "Optical coherence tomography of skin for measurement of epidermal thickness by shapelet-based image analysis," Opt. Express **12,** 5760–5769 (2004), http://www.opticsexpress.org/abstract.cfm?URI=OPEX-12-23-5760.
42. S. Jiao, R. Knighton, X. Huang, G. Gregori and C.A. Puliafito, "Simultaneous acquisition of sectional and fundus ophthalmic images with spectral-domain optical coherence tomography," Opt. Express **13,** 444–452 (2005), http://www.opticsexpress.org/abstract.cfm?URI=OPEX-13-2-444.
43. Per-Erik Danielsson, "Euclidean distance mapping", Computer Graphics and Image Processing **14** 227–248 (1980).
44. M. Mujat, C.R. Chan, B. Cense, B.H. Park, C. Joo, T. Akkin, T.C. Chen and J.F. de Boer, "Retinal nerve fiber layer thickness map determined from optical coherence tomography images," Opt. Express **12,** 9480–9491 (2005), http://www.opticsexpress.org/abstract.cfm?URI=OPEX-13-23-9480.
45. D. Cabrera Fernández, H. Salinas, and C. Puliafito, "Automated detection of retinal layer structures on optical coherence tomography images," Opt. Express **13,** 10200–10216 (2005), http://www.opticsinfobase.org/abstract.cfm?URI=oe-13-25-10200.
46. N. Kashibuchi, Y. Hirai, K. O'Goshi and H. Tagami, "Three-dimensional analyses of individual corneocytes with atomic force microscope: morphological changes related to age, location and to the pathologic skin conditions," Skin. Res. Technol. **8,** 203–211 (2002).
47. J. Welzel, M. Bruhns and H.H. Wolff, "Optical coherence tomography in contact dermatitis and psoriasis," Arch. Dermatol. Res. **295,** 50–55 (2003).
48. T. Gambichler, S. Boms, M. Stucker, G. Moussa, A. Kreuter, M. Sand, D. Sand, P. Altmeyer and K.M. Hoff-

#10151 - $15.00 USD Received 3 January 2006; revised 20 February 2006; accepted 27 February 2006

mann, "Acute skin alterations following ultraviolet radiation investigated by optical coherence tomography and histology," Arch. Dermatol. Res. **297,** 218–225 (2005).

1. Introduction

Histopathological study is an important part of dermatology, and optical coherence tomography (OCT) [1] has been widely employed in this field [2]. It has been reported that the stratum corneum and a dermal-epidermal junction are evident in OCT images [3–5]. Further appendages such as hair follicles, sebaceous glands, and sweat glands are also visible in these images [2, 6, 7]. Polarization-sensitive OCT [8], which may contrast the birefringence in human skin, was also applied in fundamental dermatological studies such as the investigation of the burnt tissue of porcine and rat skin [9, 10], where the collagen fibers in skin are denatured, thereby the birefringence are changing. Doppler OCT was also applied to skin investigations in order to visualize the blood flow under the skin [11, 12]. Further, the variation of the blood flow of a port-wine stain skin was also investigated [13].

In cosmetic science, in contrast to dermatology, it is very important to investigate the relationship between surface morphology, e.g., wrinkles, skin texture, and facial pores, and the internal structures of the skin. Wrinkles, for example, are considered to have a correlation with the structure of the basement membrane [14] and collagen fibers [15]. Thus far, video-microscopes [16] and a replication method [17] have been employed for the observation of surface morphology, while confocal microscopes [18], ultrasound tomography, and OCT [19] have been applied for noninvasive investigations of the internal structures. However, the depth measurement range of a confocal microscope, which has a higher spatial resolution than OCT, is limited. The resolution and image contrast of ultrasound tomography are not sufficient to recognize the individual structures of the skin [19]. OCT has a higher depth measurement range than confocal microscopes, and has a higher resolution than ultrasound tomography. However, in reality, conventional time-domain (TD-) OCT is only capable of two-dimensional tomographic imaging and is not sufficient for the three-dimensional morphological investigations including surface morphology and internal tomography.

Fourier domain optical coherence tomography (FD-OCT), which is also referred to as spectral domain optical coherence tomography (SD-OCT) [20, 21], is a promising alternative to TD-OCT because of its higher measurement speed [22, 23] and sensitivity [24–27] than TD-OCT. While spectrometer-based 830 nm band SD-OCT is a booming technology for retinal imaging [23, 28], 1.3 μm band is more suitable for use in dermatology and cosmetic science because of its deeper penetration than 830 nm band. However, a spectrometer-based 1.3 μm SD-OCT [29, 30] requires a line detector array that is sensitive to this band, and this line detector array is expensive and the options are limited. Swept-source (SS-) OCT [31–37], which is based on wavelength-resolved interferometry involving a wavelength scanning laser source and a point photo-detector, is emerging as an alternative to the spectrometer-based 1.3 μm SD-OCT. Recently, high-speed scanning light sources have been developed [33–35, 38], and SS-OCT systems employing these scanning light sources are applied to high-speed [32, 35, 36] and three-dimensional [36, 37] *in vivo* investigations. In this study, a custom built SS-OCT system [36] was employed for the three-dimensional tomographic imaging of *in vivo* human skin.

For cosmetic studies, we have focused on the investigation of infundibula in human facial skin. An infundibulum is a part of the sebaceous follicle, which is a type of hair follicle, and is attached to the ducts of the sebaceous glands [39]. It has been reported that the morphology of the infundibulum of a sebaceous follicle in the human face is closely related to the size of the sebaceous glands and the growth of acne [39]. Hence, the evaluation of the size and distribution of infundibula is a fundamental topic in cosmetic studies. Although infundibula are visible in

#10151 - $15.00 USD Received 3 January 2006; revised 20 February 2006; accepted 27 February 2006

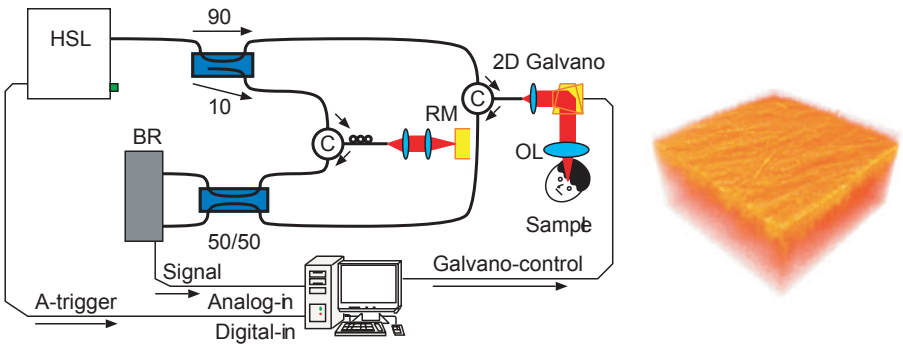

Fig. 1. A schematic of the SS-OCT system (left) and an example of the OCT volume of forehead skin *in vivo* (right). In the schematic, HSL is the high-speed wavelength scanning light source; C, the circulator; RM, the reference mirror; OL, the objective; and BR, the balanced photo-receiver.

OCT images [2], it is difficult to evaluate them morphologically because their two-dimensional images have a poor contrast. However, the morphological evaluation and screening study of infundibula are still interesting topics in the field of cosmetic science, and it is essential to develop an objective and automated method to contrast the infundibula from the OCT images.

This paper presents an algorithm that extracts the characteristic parameters and morphological structures of infundibula from a three-dimensional OCT image. This algorithm provides the mean thickness and thickness map of the epidermis, an en face shadowgram that enhances the contrast of the infundibula, the population and occupation ratio of the infundibula, and the dermal attenuation coefficient. The segmented volumes of the epidermis and infundibula are also provided by the algorithm. This algorithm is applied to the OCT volumes of human forehead skin and provides the characteristic parameters with regard to cosmetic science. The interpretations of these parameters with regard to cosmetic science are discussed. The algorithm is also applied to human cheek and human forearm skin to evaluate the portability of the algorithm. The reproducibility of the algorithm and a comparison between this algorithm and a simplified algorithm are also discussed.

2. Optical coherence tomography system

A schematic of the SS-OCT system used for human skin measurements in this study is shown in Fig. 1 (left). The light source is a high-speed wavelength scanning light source (HSL-2000, Ver. 1.0, Santec), which employs an external cavity with a polygon scanner for wavelength scanning. The light source has an A-scan rate of 20KHz, a central wavelength of 1.31 μm, and a scanning bandwidth of 110 nm. The interferometer is a fiber-based Mach-Zehnder interferometer with a 10/90 coupler, two circulators, and a 50/50 coupler. A probe unit, which is attached to one of the circulators, consists of a fiber collimator lens (11 mm focal length, Thorlabs, Inc.), a two-axis galvano mirror (Cambridge Technology), and an achromatic doublet objective lens (60 mm focal length, Thorlabs, Inc.). The maximum probe beam power is 3.0 mW, which is sufficiently below the ANSI safety standard [40]. A reference unit, which is attached to the other circulator, comprises a collimator lens, an achromatic doublet lens, and a static gold-protected mirror. The light beams reflected from the probe and the reference unit are combined by the 50/50 coupler and detected by an InGaAs balanced photo-detector (PDA10BI, Thorlabs, Inc.). As the wavelength scanning of the light source, a spectral interferometric signal is obtained. This detected spectral interference signal is amplified by an RF amplifier and sampled by an analog-

#10151 - $15.00 USD Received 3 January 2006; revised 20 February 2006; accepted 27 February 2006

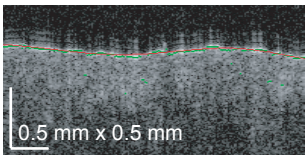

Fig. 2. A B-scan of an OCT volume. The green points indicate the maximum intensity points along the depth, and the red curve indicates the surface determined by the algorithm.

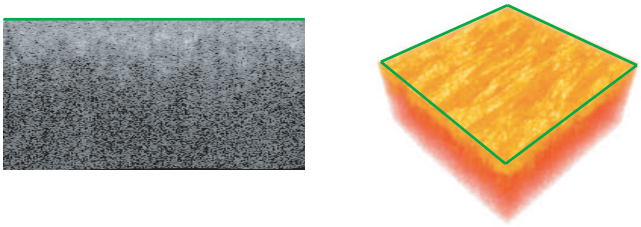

Fig. 3. A realigned B-scan (left) and the corresponding OCT volume (right). All the A-scans are realigned to flatten the sample surface. The green line and the green box indicate the flatten sample surface.

to-digital (A/D) converter. The digitized interference signal is rescaled to a frequency-even domain, and digital inverse Fourier transform yields a single A-scan (A-scan). The maximum sensitivity of our SS-OCT system is 112 dB and the depth resolution is 11.7 μm.

For three-dimensional tomography, the two-axis galvano mirror performs a two-dimensional raster scan on the probe. This SS-OCT has been previously described in detail [36].

In the measurements, we examine the human forehead skin *in vivo* with a measurement range of 4.0 mm (horizontal) $\times$ 4.0 mm (vertical) $\times$ 6.1 mm (depth) corresponding to 200 pixel $\times$ 200 pixel $\times$ 1024 pixel OCT volume, and its measurement time is 2 s. An example of the three-dimensional OCT volume is shown in Fig. 1 (right).

3. Methods

To examine the three-dimensional OCT images obtained by the abovementioned SS-OCT system, a set of algorithms was developed. From the algorithms, the following are obtained: segmented epidermis, a two-dimensional epidermal thickness map, the mean epidermal thickness, a shadowgram of infundibula, the occupation ratio and population of the infundibula, three-dimensional segments of the infundibula, and the dermal attenuation coefficient. In this section, we describe the algorithms in detail.

3.1. Surface detection

The first step of our algorithm is the surface detection of the OCT volume of the human skin. To determine the sample surface, the algorithm first locates the maximum intensity points of all the A-scans in a logarithmic cross-sectional image (B-scan), where the B-scan has been median-filtered by a 5×5 kernel. The intensity peaks corresponding to peak intensities greater than $m_p + \sigma_p$ or lower than $m_p - \sigma_p$ are rejected, and a 6th-order polynomial fits the remainder. Here, m_p is the mean peak intensity in the B-scan, and σ_p is the standard deviation of the peak intensity. This procedure is applied to all the B-scans of an OCT volume. The fitting curves

#10151 - $15.00 USD Received 3 January 2006; revised 20 February 2006; accepted 27 February 2006

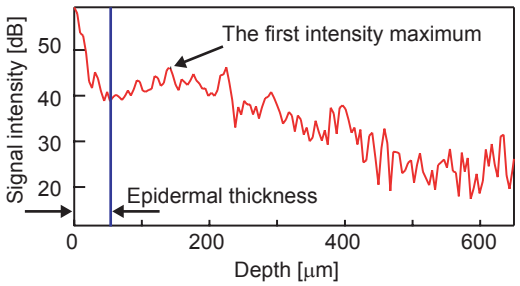

Fig. 4. A representative of the moving-averaged A-scan.

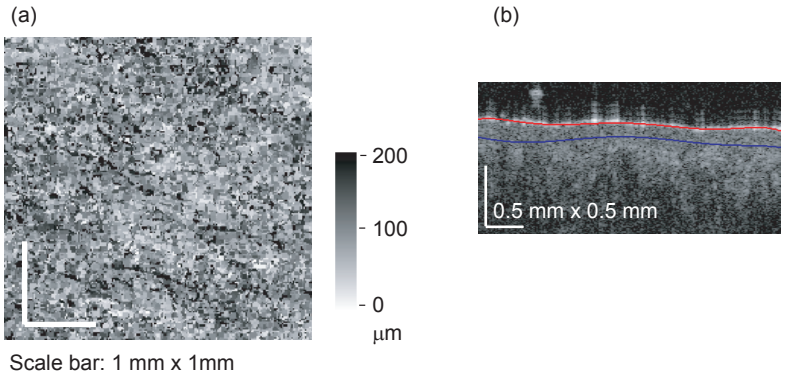

Fig. 5. (a) The distribution of epidermal thickness (epidermal thickness map), and (b) the detected surface and dermal-epidermal junction in a B-scan, where the red curve indicates the surface of the skin, and the blue curve indicates the dermal-epidermal junction.

form a surface, and the surface is then transversally sliced perpendicular to the B-scan, and a 6th-order polynomial again fits the cross-sections of the surface to smooth the result and yield a resulting surface profile as shown in Fig. 2. Subsequently, all the A-scans of the OCT volume are realigned to flatten the surface as shown in Fig. 3, and this realigned volume is considered for all the following algorithms in this study.

The standard deviation of the departures of the polynomial from the peak positions might provide a measure of the accuracy of the surface detection. In our examples, the standard deviation was typically 15 μm, which is close to the depth resolution of our SS-OCT.

3.2. Thickness map and segmentation of epidermis

The algorithm then determines the thickness distribution map and the mean thickness of the epidermis, which are important in cosmetic science and dermatology. Subsequently, the epidermis is segmented from the OCT volume by using the epidermal thickness map.

First, in the realigned OCT volume, neighboring 3×3 A-scans are moving-averaged to reduce speckle noise. In the averaged A-scan, the position of the local intensity minimum between the surface and the first intensity maximum under the surface is detected, and the distance between the surface and the local intensity minimum is defined as the epidermal thickness as shown in Fig. 4. This operation is applied to all the A-scans, resulting in an epidermal thickness map shown in Fig. 5(a), where the thickness values are adjusted by using a refractive index of 1.38. The epidermal thickness distributions of each B-scan are fitted with 6th-order polynomials to prevent spike noise, and the fitting results are averaged and provide the mean epidermal

#10151 - $15.00 USD Received 3 January 2006; revised 20 February 2006; accepted 27 February 2006

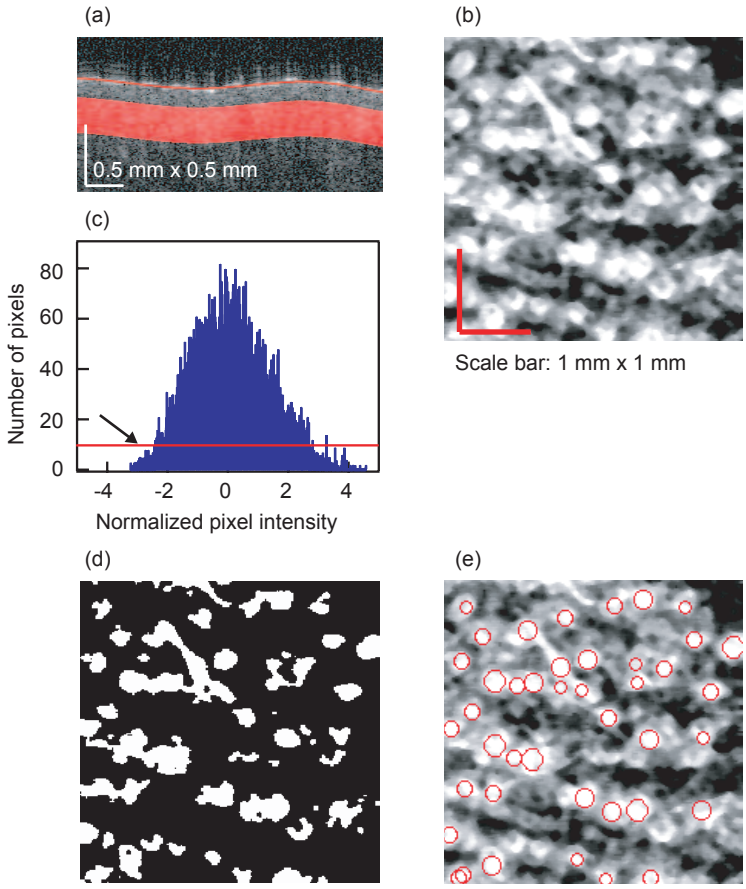

Fig. 6. (a) An example of a B-scan. The red curve indicates the detected surface and the red area indicates the domain of integration. (b) An example of the en face shadowgram; white corresponds to low signal intensity and black corresponds to high signal intensity. The white spots indicate the infundibula. (c) The histogram of the shadowgram (b). Pixel intensities are normalized by the mean and standard deviation of the histogram. The distributions under the red line (10% of the maximum) were not considered while calculating the mean and standard deviation. (d) A binary map of the distribution of the infundibula. (e) The red circles indicate the island spots detected as circles by the Danielsson distance mapping algorithm. The circles are superimposed on the shadowgram (b).

thickness. Subsequently, this thickness map is employed to segment the epidermis from the OCT as shown in Fig. 5(b).

3.3. Shadowgram and statistic properties of infundibula

In the OCT images, an infundibulum appears as a low signal intensity segment because of its weak scattering property [2]. In our algorithm, the distribution of the infundibula is analyzed by an en-face-oriented algorithm.

In this algorithm, the OCT volume that is first realigned to flatten the surface as described in section 3.1, is integrated along the depth from 100 μm to 300 μm on a linear scale, where these depths are adjusted by using a refractive index of 1.38. The integration area is indicated by the red belt in Fig. 6(a). This integration provides an en face image of the infundibula with enhanced

#10151 - $15.00 USD Received 3 January 2006; revised 20 February 2006; accepted 27 February 2006

contrast as show in Fig. 6(b). This image is similar to the shadowgram demonstrated by Jiao *et al.* for contrasting retinal vessels [42]. Because the infundibula appear as low signal intensity segments in the OCT image, the low intensity (white) spots in the shadowgram correspond to the infundibula.

The histogram of the shadowgram with 2000 bins is then employed to determine the threshold in order to obtain a binary contrast of the infundibula. An example of the histogram is shown in Fig. 6(c). Because the infundibula exhibit weak scattering, the side lobe of the low intensity pixels indicated by an arrow corresponds to the infundibula. The mean (m_h) and standard deviation (σ_h) of the histogram are then calculated; the side lobes below the 10% of the maximum of the histogram (the red line in the figure) are not considered to calculate the mean and the standard deviation. The threshold s for segmenting the infundibula is determined as

$$s = m_h - \alpha\sigma_h \tag{1}$$

where α is a constant dependent on the region of measurement. For forehead skin, α is 1. This threshold and the shadowgram provide an en face binary map of the infundibula as shown in Fig. 6(d), and the binary map provides the occupation ratio of the infundibula.

Subsequently, the Danielsson distance mapping algorithm [43], which detects the island spots in a binary image as circles, is applied to the binary map. The circles detected by the Danielsson distance mapping algorithm are superimposed on the shadowgram as shown in Fig. 6(e). The low intensity island spots (white spots) on the binary map correspond to the infundibula, hence, the given circles also correspond to the infundibula. Finally, the population of the infundibula is obtained by this mapping algorithm.

3.4. Three-dimensional segmentation of the infundibula

Recently, a B-scan-oriented segmentation algorithm was successfully demonstrated for retinal OCT [44, 45]. The important structures of the retina are mostly depth-oriented layers, and it is reasonable to apply such a B-scan-oriented segmentation algorithm. On the other hand, infundibula are immersed in the skin as isolated spots, hence, it is difficult to segment them by the B-scan-oriented algorithm. Furthermore, a B-scan-oriented thresholding segmentation algorithm is not always suitable, although the infundibula exhibit a weaker scattering than others parts of skin, because the depth-dependent signal decay of an OCT image due to sample scattering disturbs this thresholding. Therefore, we employed an en-face-oriented thresholding method to segment the infundibula, where each en face image is extracted from the realigned OCT volume, and has a constant depth from the surface.

In this segmentation, an en face image at a particular depth from the surface is extracted from the OCT volume. A histogram-based thresholding method, which is identical to the method described in section 3.3, is applied, and the threshold is obtained. From the threshold, a binary mask to segment the infundibula at this depth is obtained. This thresholding algorithm is applied to the en face images at every depth of the OCT volume, and this finally yields a three-dimensional binary mask to extract the infundibula from the OCT volume.

Based on this three-dimensional binary mask and the epidermal segmentation described in section 3.2, three segments of the skin can be distinguished from a single OCT volume. Figure 7(a) and its movie show sequences of B-scans extracted from an OCT volume. The upper image is the original OCT image and the lower image is the segmented OCT image by the above-mentioned procedure in which the blue area indicates the epidermis and the green areas indicate the infundibula. The infundibula are visible in the original OCT image as low scattering regions [2], and the correspondence between the infundibula in the original OCT and those of automatically segmented OCT are evident in the movie. Figure 7(b) shows the corresponding shadowgram. Figure 8(a) shows a non-segmented OCT volume and Fig. 8(b) shows

#10151 - $15.00 USD Received 3 January 2006; revised 20 February 2006; accepted 27 February 2006

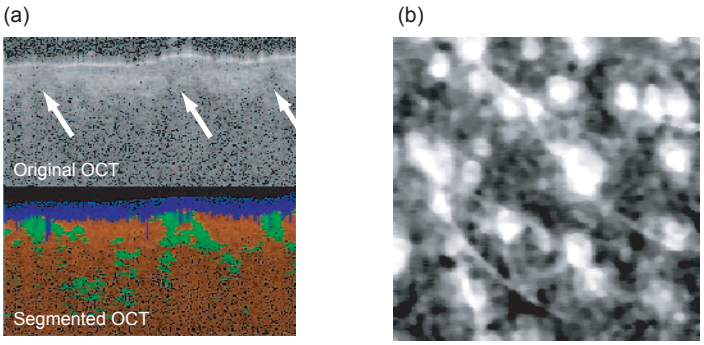

Fig. 7. (a) A B-scan of the original OCT volume and that of the segmented OCT volume. The white arrows and the green spots indicate the infundibula. (b) Corresponding shadowgram. Click the figure (a) to see a movie (2.4 MB).

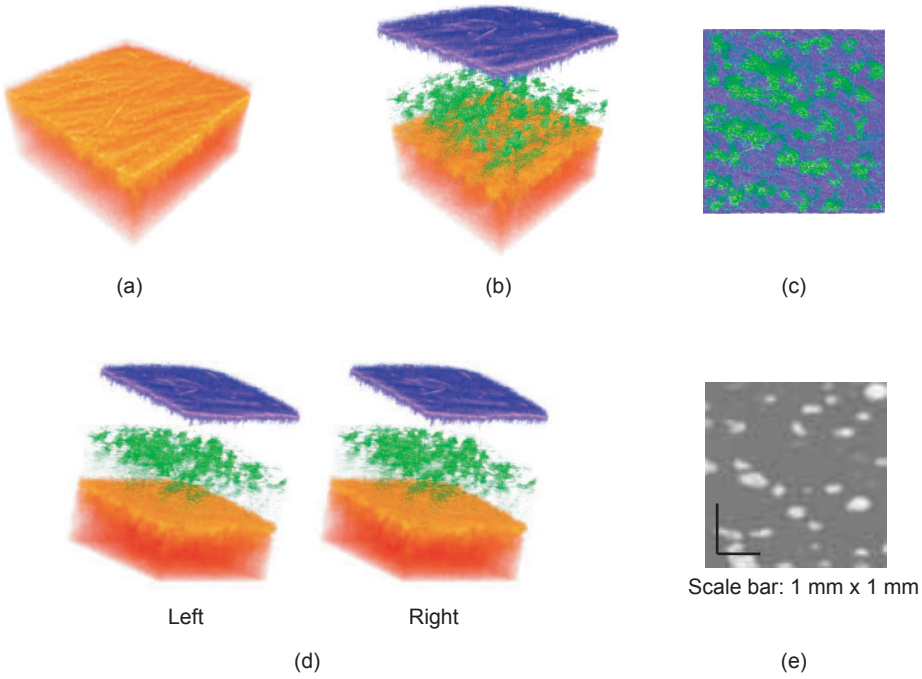

Fig. 8. (a) The original OCT volume, (b) a segmented OCT volume, and (c) the top view of the segmented OCT volume. The blue, green, and orange volumes in the right figure correspond to the segments of the epidermis, infundibula, and the remaining volume, respectively. In (c), the infundibula are superimposed on the epidermis. (d) A stereogram of (b) for three-dimensional understanding of the structure. (e) A sebum absorbent tape image. The white spots represent the absorbed sebum. Click the figure (b) to see a movie (1.9 MB).

#10151 - $15.00 USD Received 3 January 2006; revised 20 February 2006; accepted 27 February 2006

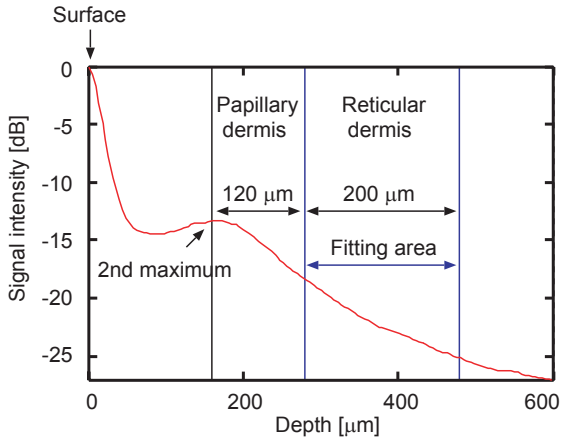

Fig. 9. An example of the attenuation curve. The portion of the curve between the blue lines is fitted by a linear line to obtain the attenuation coefficient.

the corresponding segmented OCT volume, where the epidermis (a blue volume), infundibula (green volumes), and remaining volume (an orange volume) are shown at different positions with different color maps. Figure 8(c) is the top view of the volume of Fig. 8(b), where the infundibula are superimposed on the epidermis. Figure 8(d) is a stereogram of Fig. 8(b) for three dimensional understanding of the structure.

3.5. Dermal attenuation coefficient

We determined the dermal attenuation coefficient from the OCT volume. For this purpose, all the A-scans of the realigned OCT volume are averaged on a linear scale. The averaged A-scan is represented by a logarithmic scale as shown in Fig. 9, and a linear line fits a portion of the A-scan. This portion has a depth of 200 μm and starts from a 120 μm in depth to the second maximum peak (see Fig. 9). This portion corresponds to the reticular dermis, while the superior 120 μm-thickness layer corresponds to papillary dermis, where the depth values are again adjusted by using a refractive index of 1.38. This fitting line provides the dermal attenuation coefficient μ as

$$I(z) \propto e^{-2(\mu+\mu_{\mathrm{OCT}})z} \tag{2}$$

where z is the depth position and $I(z)$ is the signal intensity of the averaged A-scan. μ_{OCT} is a system attenuation coefficient dominated by the resolution of spectral sampling of SS-OCT and the instantaneous linewidth of the wavelength scanning light source, and is 1.7 cm $^{-1}$ in our SS-OCT [36]. The dermal attenuation coefficient is related with the absorption coefficient and the scattering coefficient of the dermis, and can be considered as a measure of the translucency of skin [47].

4. Measurements and results

4.1. Segments and shadowgrams

To validate this method, we examined five volunteers. The subjects are Asian males whose ages range from 22 to 44, and the forehead skins of these subjects are measured by SS-OCT. Figure 10 shows the shadowgrams, and the segmented volumes of the epidermis, the infundibula and the remaining volumes of the three representative subjects. For all the calculations, the parameters of the algorithm do not change. The high stability of this automated algorithm is reflected

#10151 - $15.00 USD Received 3 January 2006; revised 20 February 2006; accepted 27 February 2006

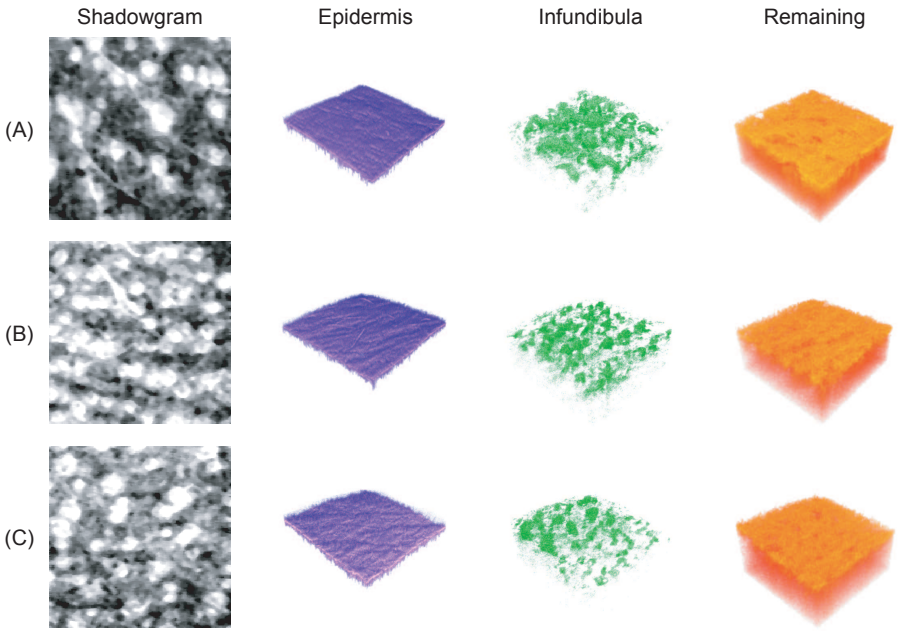

Fig. 10. Shadowgrams and segmented OCT volumes of the forehead skin of three representative subjects.

in the results, and this method might be applicable to large-scale studies.

The epidermal volumes provide intuitive understanding of epidermal thickness and surface morphology. The shapes and distributions of the infundibula are evident from the segmented volumes. The shadowgrams give the distributions of the infundibula, and the individual variations of the distribution are evident.

On the epidermis of subject-(B), the hollows on the surface are evident as shown in Fig. 10. The infundibula co-localizing at the hollows are observed in the corresponding segmented volumes of the infundibula.

4.2. Characteristic parameters

Table 1. The mean epidermal thicknesses, populations and occupation ratios of the infundibula, and dermal attenuation coefficients of the five subjects.

	Mean epidermal thickness (μm)	Infundibulum population (cm^{-2})	Infundibulum occupation ratio (%)	Dermal attenuation coefficient (cm^{-1})
Subject 1	100 ± 28	225	20.9	31.7
Subject 2	90 ± 8	194	19.9	20.5
Subject 3	100 ± 3	181	21.6	24.8
Subject 4	100 ± 29	181	20.3	27.5
Subject 5	90 ± 10	188	22.4	31.9
Mean	98	194	21.0	27.3

The characteristic parameters of the five subjects are shown in Table 1. The epidermal thick-

#10151 - $15.00 USD Received 3 January 2006; revised 20 February 2006; accepted 27 February 2006

nesses are adjusted by using a refractive index of 1.38. The obtained epidermal thicknesses [41], the populations of the infundibula [39], and the dermal attenuation coefficients [47] are in good agreement with previously reported values. The populations of the infundibula were also manually counted from the original OCT volumes, and the root-mean-square error between the manually counted values and the automatically counted values was 18.8%. Taking the errors of the manual count into account, it is reasonable to think that the automated algorithm correctly determines the population of infundibula.

5. Discussions

5.1. Dermatological interpretations of the segments and parameters

It is known that the size of an infundibulum is related to that of a sebaceous gland, and the structural changes of an infundibulum accompany the growth of acne [39]. Thus, the structural observation of infundibula with segmented OCT volumes will be a useful tool for understanding these dermatological dynamics.

Sebaceous glands are classified into two types: active and inactive. The active gland secretes sebum while the inactive gland does not. The distribution of the infundibula measured by our method is related to both active and inactive glands. This distribution and the distribution of active glands measured by other method, such as a sebum absorbent tape, will contribute to understanding the dynamics of sebum secretion. Figure 8(e) shows an example of the sebum absorbent tape (Sebutape, CuDerm Corporation, Texas) image of human forehead skin of close area of the OCT measurement in Figs. 8(a)-(c). The difference of the populations of the spots between the sebum absorbent tape image and the segmented volume/shadowgram may account for the population difference between the active and inactive glands.

It is known that secreted sebum is stored in the ducts of sebaceous glands and the infundibula. Therefore, the infundibulum occupation ratio might have a relation with the rate at which sebum is re-formed on the face after washing.

It has been reported that due to cutaneous inflammatory diseases, the epidermis thickens [47] and the stratum corneum becomes abnormal [46]. Hence, the mean epidermal thickness can be considered as a quantitative parameter for skin diagnosis, and two-dimensional epidermal thickness maps will help in understanding the mechanism of development of cutaneous inflammatory diseases.

It has been reported that the scattering coefficient is altered by the exposure to ultraviolet radiation [48]. Since the dermal attenuation coefficient obtained in section 3.5 is well related with the scattering coefficient, it might be useful to study the photoaging of skin.

5.2. Portability of the algorithm

To examine the portability of this algorithm, we applied it to forearm skin and cheek skin. α in Eq. (1) is selected as 2 for the forearm skin and 0.5 for the cheek skin.

The algorithm was successfully applied to several OCT volumes of the forearm skin and the cheek skin. Table 2 shows some examples of the charateristic parameters of the forearm skin and the cheek skin, and Fig. 11 shows examples of shadowgrams and the segmented OCT volumes. In the measurements, the forearm rests on a glass plate in order to fix the position to be measured. The shadowgram and the segmented volume of the infundibula show that the population of the infundibula of the forearm skin is considerably lower than that of the forehead skin and the cheek skin as previousely reported [39]. The mean infundibulum population of the forearm skin of the five subjects is automatically counted as 44 ± 20 counts/cm^2 by the algorithm, which agrees with the previousely reported value of 50 counts/cm^2 [39]. From the shadowgram and the infundibulum segments of the cheek skin, it is evident that both small and big infundibula exist on the cheek.

#10151 - $15.00 USD Received 3 January 2006; revised 20 February 2006; accepted 27 February 2006

Table 2. The mean epidermal thicknesses (MET), the infundibulum populations (IP) and infundibulum occupation ratios (OP) of the five subjects.

	MET (μm)	IP (cm^{-2})	OP (%)	MET (μm)	IP (cm^{-2})	OP (%)
	Forearm			Cheek		
Subject 1	70 ± 20	25	3.9	100 ± 30	369	33.8
Subject 2	63 ± 5	81	8.9	60 ± 23	435	35.1
Subject 3	65 ± 5	38	7.9	60 ± 30	462	35.6
Subject 4	96 ± 4	31	4.8	90 ± 20	344	34.3
Subject 5	76 ± 6	44	6.1	70 ± 20	462	35.6
Mean	72	44	6.3	76	412	34.7

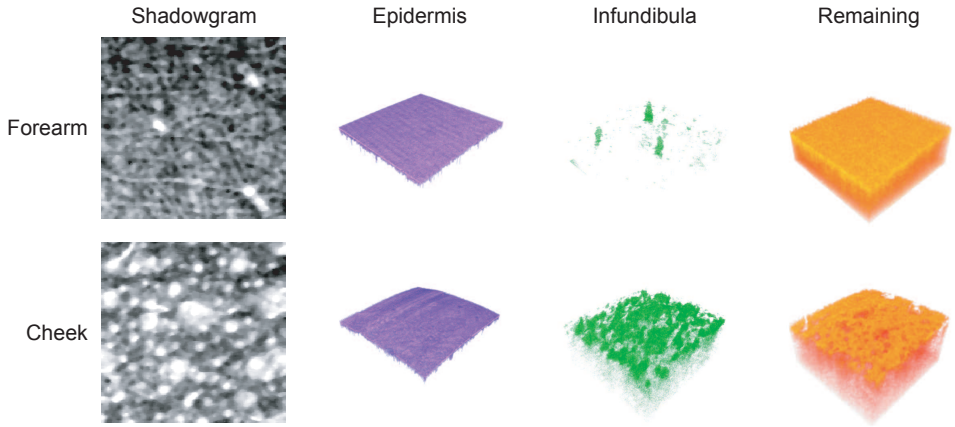

Fig. 11. Shadowgrams and segmented OCT volumes of the forearm skin and the cheek skin.

5.3. *Reproducibility of the algorithm*

Table 3. The mean epidermal thicknesses, populations and occupation ratios of the infundibula, and dermal attenuation coefficients of a single subject. The measurements were repeated ten times, and the unbiased standard deviations of each parameter are also shown.

	Mean epidermal thickness (μm)	Infundibulum population (cm^{-2})	Infundibulum occupation ratio (%)	Dermal attenuation coefficient (cm^{-1})
Forehead	$98.3 \pm 5.7\%$	$239 \pm 15.6\%$	$19.7 \pm 3.2\%$	$34.4 \pm 5.3\%$
Forearm	$67.6 \pm 4.1\%$	$49 \pm 30.4\%$	$7.5 \pm 13.3\%$	$51.6 \pm 5.2\%$
Cheek	$66.8 \pm 5.8\%$	$372 \pm 9.8\%$	$34.4 \pm 1.8\%$	$45.2 \pm 7.9\%$

To evaluate the reproducibility of the algorithm, a single subject was examined 10 times. The size of the measurement area was 4 mm times 4 mm, and the measurement positions were randomly selected from a 20 mm time 20 mm region. The mean parameters and their unbiased standard deviations are shown in Table 3.

Most of the standard deviations are around 5% and they are resonably small. The standard deviations of the populations of infundibula are in the range of 10% to 30%, and are slightly

#10151 - $15.00 USD Received 3 January 2006; revised 20 February 2006; accepted 27 February 2006

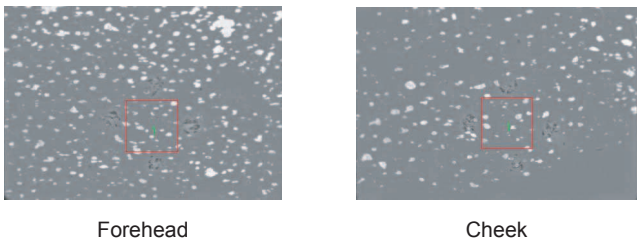

Fig. 12. Sebum absorbent tape images of the forehead skin and the cheek skin of a subject of Table 3. The red squares indicate the size of a single OCT volume (4 mm times 4 mm).

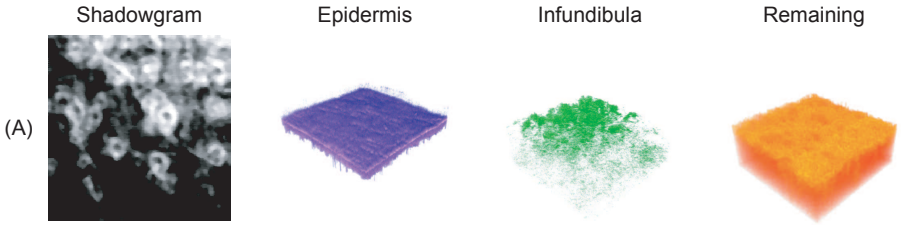

Fig. 13. The shadowgrams and segmented OCT volumes produced by a simplified algorithm. The raw OCT volume is identical to that of subject (A) shown in Fig. 10.

larger than others. However, the sebum absorbent tape images of the forehead skin and cheek skin of the subject shown in Fig. 12 indicate the nonuniform distributions of the sebaceous glands, and it is reasonable to think that the real distribution of the infundibula itself also has nonuniformity.

5.4. Constant depth algorithm versus constant delay algorithm

In the method described in sections 3.4 and 3.3, the algorithm used en face OCT slices at a constant depth from the surface determined by another algorithm described in section 3.1 in order to avoid the problems related to the depth-dependent signal decay of OCT images. An algorithm that uses en face OCT slices at a constant depth from the zero-delay point, i.e., using a non-realigned OCT volume, seemed to be a simpler alternative to our algorithm. To compare these two algorithms, we apply the latter to the OCT volume of subject (A) show in Fig. 10.

In the results shown in Fig. 13, the infundibula appear to be localized in the right upper side of the shadowgram. This localization is an artifact due to the departure of the sample surface from a constant delay plane and consequent variation of signal offsets in the en face OCT images. The result indicates that this simple algorithm did not work correctly, and it is reasonable to use our algorithm.

6. Conclusions

A set of fully automated algorithms which was specialized to analyze three-dimensional OCT volumes of human skin was developed. A surface detection algorithm first determined the surface of the OCT volume, and subsequently, thickness map and the mean thickness of the epidermis were obtained. An en face shadowgram of the OCT volume, which displays infundibula with higher contrast than conventional OCT images, was produced by an algorithm that uses the detected surface. A histogram-based thresholding was applied to the shadowgram and this thresholding provided a binary map of the distribution of the infundibula. The occupation ratio

#10151 - $15.00 USD Received 3 January 2006; revised 20 February 2006; accepted 27 February 2006

of the infundibula is obtained from the binary map. Circular structures in the binary map were obtained by the Danielsson distance mapping algorithm, and it provided the population of the infundibula. The dermal attenuation coefficient was also provided from the OCT volume as a measure of skin texture.

The OCT volume was sliced into en face OCT slices at constant depths from the sample surface. The histogram-based thresholding was applied to each individual slice to provide a three-dimensional segmented volume of the infundibula, while the segmented volume of the epidermis was obtained by using the epidermal thickness map.

The algorithm set was applied to several OCT volumes of human forehead skin, and the high stability of the algorithm set was confirmed. The portability of the algorithm set was also confirmed by its application to other parts of the human skin, such as forearm skin and and cheek skin. The reproducibility of the algorithm set was examined by repetitive measurement of a single subject, and the algorithm set showed reasonable reproducibility. A comparison between our method and a simple method was also discussed, and this comparison showed the advantages of our method.

The forehead skins of five volunteers were examined, and the their characteristic parameters of their skin were in agreement with the previous reports. Dermatological interpretations of the characteristic parameters were also discussed.

Acknowledgments

We would like to thank Masahiro Akiba, Atsushi Morosawa and Changho Chong for their discussions with regard to the SS-OCT system. We also thank Gouki Aoki, Yoshifumi Nakamura, Youngjoo Hong, and Chia-Wei Sun for their technical and scientific contributions and helpful advices. Yasuaki Hori is visiting from the Department of Mechanical Science and Bioengineering, Graduate School of Engineering Science, Osaka University, Osaka, Japan. This research is partially supported by a Grant-in-aid for Scientific Research 15760026 from the Japan Society for the Promotion of Science (JSPS), Japan Science and Technology Agency, and the Special Research Project of Nanoscience at University of Tsukuba. Masahiro Yamanari and Shuichi Makita are supported by JSPS through a contract under the Promotion of Creative Interdisciplinary Materials Science for Novel Functions, 21st Century Center of Excellence (COE) Program.

#10151 - $15.00 USD Received 3 January 2006; revised 20 February 2006; accepted 27 February 2006